The importance of surface adsorbates in solution-processed thermoelectric materials: the case of SnSe

*Yu Liu,[#] Mariano Calcabrini[#] Yuan Yu, Aziz Genç, Cheng Chang, Tommaso Costanzo, Tobias Kleinhanns, Seungho Lee, Jordi Llorca, Oana Cojocaru-Mirédin, Maria Ibáñez**

Dr. Y. Liu, M. Calcabrini, Dr. C. Chang, Dr. T. Constanzo, T. Kleinhanns, S. Lee, Prof. Maria Ibáñez
IST Austria, Am Campus 1
3400 Klosterneuburg, Austria.
E-mail: mibanez@ist.ac.at

[#] These authors contributed equally to this work.

Dr. Y. Yu, Prof. O. Cojocaru-Mirédin
RWTH Aachen, I. Physikalisches Institut (IA), Sommerfeldstraße 14
52074 Aachen, Germany.

Prof. A. Genç
Department of Materials Science and Engineering, Faculty of Engineering, Izmir Institute of Technology
İzmir 35430, Turkey

Prof. J. Lorca
Institute of Energy Technologies, Department of Chemical Engineering and Barcelona Research Center in Multiscale Science and Engineering, Universitat Politècnica de Catalunya
08019 Barcelona, Spain.

Keywords: SnSe, sodium, solution-processed, grain boundary, energy filtering, liquid-phase sintering, thermoelectrics

Abstract: Solution synthesis of nanoparticles (NP) emerged as an alternative to prepare powders for thermoelectric materials with less demanding processing conditions than conventional melting and mechanical alloying. However, when NPs are synthesized in solution, their nucleation and growth occur in the presence of reaction regulating compounds that interact with the NP surface, yielding NPs with specific surface adsorbates. In surfactant-assisted colloidal synthesis, surface adsorbates are known and linked to detrimental effects due to their insulating nature. Conversely, in the so-called surfactant-free syntheses, their presence and impact on the final material have been greatly overlooked. Here, we demonstrate that ionic adsorbates are unavoidable in surfactant-free synthesis and play a crucial role in the material microstructure evolution and thermoelectric properties. In particular, we study polycrystalline SnSe produce from NPs synthesized in polar solvents. This work shows that the common use of sodium salts as precursors yields unavoidably significant quantities of sodium in the final material. Based on the fundamentals of colloidal science, we explain that Na is an inevitable impurity as Na ions are electrostatically adsorbed at the NP surface to preserve charge neutrality. In the sintered pellets, Na^+ is present within the matrix as dopants, in dislocations,

precipitates, and forming grain boundary complexions. The interfaces created between SnSe and Na-rich phases lead to energy filtering effects, enhancing the Seebeck coefficient.
These results can be extended to other colloidal syntheses in polar media and highlight the importance of considering all the possible unintentional impurities to establish proper structure-property relationships and control material properties in solution-processed thermoelectric materials.

1. Introduction

Thermoelectric devices reversibly convert heat into electricity both for power harvesting and for active cooling and heating. The efficiency of a thermoelectric device is determined by the temperature-dependent properties of the materials that constitute it. These are summarized in the thermoelectric figure of merit of each material, $zT = S^2 \sigma \kappa^{-1} T$, that combines Seebeck coefficient (S), electrical conductivity (σ), thermal conductivity (κ) and absolute temperature (T).[1]

The materials used in conventional thermoelectric devices are dense, polycrystalline inorganic semiconductors. Commonly, the processing of such materials has two steps: preparation of the semiconductor in powder form and the consolidation of the powder into a dense sample. The most common route to prepare powders among the thermoelectric community is through melting or mechanical alloying.[2] Alternatively, solution methods to produce micro- and nanoparticle (NP)-based powders with much less demanding conditions (*e.g.* lower reagent purity, lower temperatures, shorter reaction times) have been explored to reduce the powder production costs.[1,3] Furthermore, solution methods provide opportunities to produce powders with controlled features, such as average crystalline size, shape, composition, and crystal phase, to tune the consolidation process modifying the final material properties.[4,5] The synthesis of NPs in solution also enables an exquisite control over surface properties, such as faceting and surface composition at the atomic level.[6] Lastly, solution-based methods allow extended device fabrication versatility, including flexible, conformable, and rigid modules with customized geometries.[7,8]

To date, solution-based syntheses lead to several bulk materials with state-of-the-art performances, as is the case of PbS,[5] $Bi_{0.5}Sb_{1.5}Te_3$[9], and SnSe,[3] proving the potential of the strategy. Unlike solid-state processed powders, when dealing with NPs synthesized in solution, one should pay special attention to the role of surface species. In a non-vacuum environment, surfaces are usually covered by adsorbates.[10] For solids prepared from solution-processed NPs, the composition, chemical stability, and bonding nature of surface species play a role in the sintering process, and reaction byproducts can determine the final properties of the consolidated material.

Surface species are carefully considered in surfactant-assisted colloidal synthesis because of the insulating nature of the generally used long-chain aliphatic surfactants[11] and the consequent detrimental effects on thermoelectric performance.[12] In such cases, the surfactants have to be removed to enhance the electrical conductivity. The most common strategy to do so is thermal decomposition, but this results in the presence of residual carbon in the final solid.[13–15] Alternatively, surfactants can be exchanged with volatile compounds[16] or even inorganic species[17] that can further tune material properties.[15,18,19] In other synthetic methods, however, surface adsorbates are usually neglected. This is the case for the so-called surfactant-free methods,[3,20–32] the most widely used to produce thermoelectric powders. The vast majority of these reports do not include surface treatments since the NPs are considered "naked".[30,33,34] This is a miss conception as depending on the NP composition and surface termination, different species are adsorbed at the NP surface. Such surface adsorbates need to be identified to understand their role in the thermoelectric properties. Despite this, to the best of our knowledge, no reports have considered the role of adsorbates in surfactant-free solution-processed thermoelectric materials.

Here, we study the effect of surface adsorbates in polycrystalline SnSe produced from solution-synthesized NPs. SnSe highest zT obtained so far in p-type SnSe is ~2.6 at 923 K along the b

axis in SnSe single crystals;[40] and ~2.8 at 773 K along the out-of-plane direction in Br-doped n-type SnSe single crystal.[41] The superb performance of these materials is linked to the strong anharmonicity of the Sn-Se bonds that translates into ultralow thermal conductivities,[42,43] and to its multiple bands that can be accessed by doping to optimize its electronic properties.[35] However, the high cost, tedious production of single crystals, and their poor mechanical properties limit the large-scale use of SnSe in thermoelectric devices. Therefore, different strategies to produce polycrystalline SnSe with comparable performance are being explored,[44–48] including solution processing methods.[3,20,49–53,21–23,25–28,32] In this work, we identify the surface species resulting in the aqueous synthesis of SnSe NPs, and demonstrate their effects on the sintering process and the thermoelectric properties.

2. Material synthesis: from SnSe powder to bulk SnSe

The table below shows the most common reactants to synthesize SnSe in solution that yield state-of-the-art performances (Table 1). SnSe NPs are usually prepared in polar media (water or ethylene glycol, EG) using $SnCl_2$ and Se, SeO_2, or Na_2SeO_3 as precursors. Additionally, to ensure precursor solubility in the media, redox agents and acids or bases are used, generally, these are Na^+ salts, as highlighted in Table 1. In all these reactions, soluble Sn^{2+} and Se^{2-} species precipitate, forming SnSe NPs. Herein, we selected the simplest and most cost-effective synthetic method (i.e. normal pressure and water as solvent) as a prototypical reaction and used a slightly modified synthesis reported by Gregory *et al.*[31]

Table 1. Summary of the state-of-art thermoelectric performance of p-type doped polycrystalline SnSe from solution-processed methods: including precursors, solvents, reaction temperature (T), reaction time (t), sintering conditions, and peak zT values (zT_{max}).

Material	Precursors, solvent	zT_{max}
$Sn_{0.96}Ga_{0.04}Se$[20]	$SnCl_2{\cdot}2H_2O$, $GaCl_3$, NaOH, Se, H_2O	2.2 (873 K)
$Sn_{0.98}Pb_{0.01}Zn_{0.01}Se$[27]	$SnCl_2{\cdot}2H_2O$, $PbCl_2$, $ZnCl_2$, NaOH, Se, H_2O	2.2 (873 K)
$Sn_{0.95}Se$[50]	$SnCl_2{\cdot}2H_2O$, NaOH, Se, H_2O	2.1 (873 K)
$Sn_{0.97}Ge_{0.03}Se$[3]	$SnCl_2{\cdot}2H_2O$, GeI_4, NaOH, Se, H_2O	2.1 (873 k)
$Sn_{0.99}Pb_{0.01}$Se-Se QDs[51]	$SnCl_2{\cdot}2H_2O$, $PbCl_2$, NaOH, Se, H_2O	2.0 (873 K)

$Sn_{0.96}Pb_{0.01}Cd_{0.03}Se$[22]	$SnCl_2{\cdot}2H_2O$, $PbCl_2$, $CdCl_2$, NaOH, Se, H_2O	1.9 (873 K)
$Sn_{0.948}Cd_{0.023}Se$[52]	$SnCl_2{\cdot}2H_2O$, $CdCl_2$, Na_2SeO_3, NaOH, EG	1.7 (823 K)
SnSe-4%$InSe_y$[54]	$SnCl_2{\cdot}2H_2O$, $InCl_3{\cdot}4H_2O$, Na_2SeO_3, NaOH, EG	1.7 (823 K)
SnSe-1%PbSe[23]	$SnCl_2{\cdot}2H_2O$, $PbCl_2$, NaOH, Se, H_2O	1.7 (873 K)
NaOH-$Sn_{1-x}Se$[28]	$SnCl_2$, Na_2SeO_3, NaOH, EG	1.5 (823 K)
$Sn_{0.882}Cu_{0.118}Se$[32]	$SnCl_2{\cdot}2H_2O$, $CuCl_2$, Na_2SeO_3, NaOH, EG	1.41 (823 K)
SnSe-15%Te NWs[49]	$SnCl_2{\cdot}2H_2O$, $NaBH_4$, NaOH, Se, H_2O	1.4 (790 K)
$Sn_{0.98}Se$[50]	$SnCl_2{\cdot}2H_2O$, Na_2SeO_3, NaOH, EG	1.36 (823 K)
$SnSe_{0.90}Te_{0.1}$[55]	$SnCl_2{\cdot}2H_2O$, Na_2SeO_3, Na_2TeO_3, NaOH, EG	1.1 (800 K)
$Sn_{0.99}Cu_{0.01}Se$[26]	$SnCl_2{\cdot}2H_2O$, CuCl, NaOH, Se, H_2O	1.2 (873 K)
$SnSe_{0.9}S_{0.1}$[21]	$SnCl_2{\cdot}2H_2O$, Na_2S, $NaBH_4$, NaOH, Se, H_2O	1.16 (923 K)

In the chosen synthetic procedure, $NaBH_4$ is first dissolved in water, and Se powder is slowly added to form HSe^-. In parallel, NaOH and $SnCl_2{\cdot}2H_2O$ are dissolved in water and the solution is heated to its boiling point. At this temperature, the freshly prepared Se-solution is rapidly injected. Upon injection, the reaction mixture turns black, indicating NP formation. After that, the reaction mixture is kept under reflux for additional 2 h. The as-synthetized NPs are purified by precipitation/redispersion with water and ethanol and then dried under vacuum overnight at room temperature. Afterwards, NP powder is annealed in forming gas (95% N_2 + 5% H_2) to remove oxides.[44] Finally, the annealed powders are sintered into cylindrical pellets using a spark plasma sintering system. Throughout the process, X-ray diffraction (XRD) is used to verify that the product is pure phase orthorhombic SnSe (**Figure 1**). From NP synthesis to the pellet formation, the experimental details can be found in the methods section.

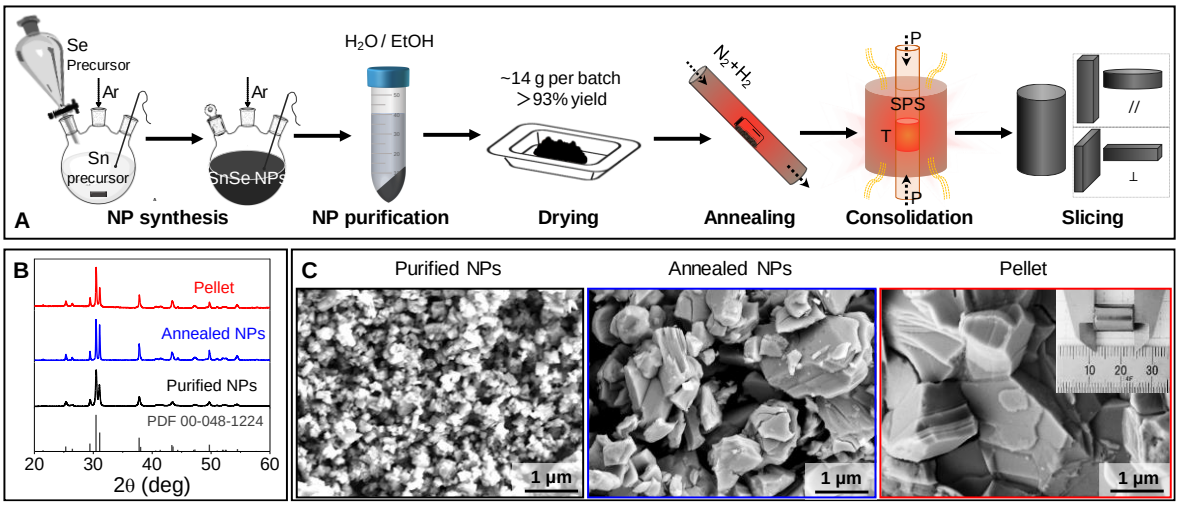

Figure 1. A) Scheme of the processing steps of SnSe pellets. B) XRD patterns of initial SnSe NPs, annealed NPs, and sintered pellet along the out-of-plane direction, including the reference PDF 00-048-1224. C) Corresponding representative SEM micrographs of the material in the different processing steps. The inset shows a dense SnSe cylindrical pellet.

3. NP properties

To have a comprehensive understanding of the sintered material and its formation, we first analyzed the NPs in detail. Scanning electron microscopy (SEM) and transmission electron microscopy (TEM) showed that the NPs have a rectangular shape with an average lateral size of ca. 150 nm (Figure 1C and 2A). High-resolution TEM (HRTEM) analysis confirmed the SnSe orthorhombic structure (space group *Pnma*) with lattice parameters a=11.5156 Å, b=4.1571 Å, and c=4.4302 Å observed by XRD. We further performed energy-dispersive X-ray spectroscopy (EDS) analysis to study the composition of the particles and found that the SnSe NPs are slightly Se-rich (Figure S1). Moreover, EDS revealed that the particles contained Na, while neither Cl (from $SnCl_2$) nor B (from the excess BH_4^-) were detected, indicating that the washing effectively removes byproducts and excess reagents (**Figure 2**B). X-ray photoemission spectroscopy (XPS, Figure S3) analysis suggests that most of the Na is at the NP surface, yet we cannot discard its partial presence within the SnSe NPs. In the Se 3d XPS region, four peaks can be deconvoluted. These correspond to the $3d^{3/2}$ and $3d^{5/2}$ emission peaks

of Se in two different oxidation states. Se^{2-}, from SnSe, is observed at low binding energies while at higher energies, more oxidized Se species are present, with an oxidation state closer to 0.[21],[57] We speculate that these species are polyselenides (Se_x^{2-}), formed by partial oxidation of the NP surface during washing, as has been observed for Cu_2Se NPs.[58–60] During the synthesis, Na^+ is a spectator ion that compensates the charge of the reactive ions (OH^-, BH_4^-, HSe^-, etc.) but does not react in any way. However, its presence in the washed NPs indicates that Na^+ are adsorbed at the surface. To understand the nature of the adsorption, we performed electrophoretic mobility measurements and determined that SnSe NPs are negatively charged (zeta-potential = -22 ± 5 Mv, Figure 2C) consistent with the Se-rich surface as determined by EDS (Figure S1). These results indicate that, in solution, the NPs are surrounded by a layer (Stern layer) of strongly bound cations (Na^+) and a second layer of loosely bound ions (diffuse layer) composed mostly of cations (Na^+) and some anions (OH^-, HSe^-) (Figure 2C). During washing, most of the anions are washed away (final pH = 10), but cations remain to ensure charge neutrality, explaining the presence of Na+ in the surface of the NPs (Na-SnSe, Figure 2D).

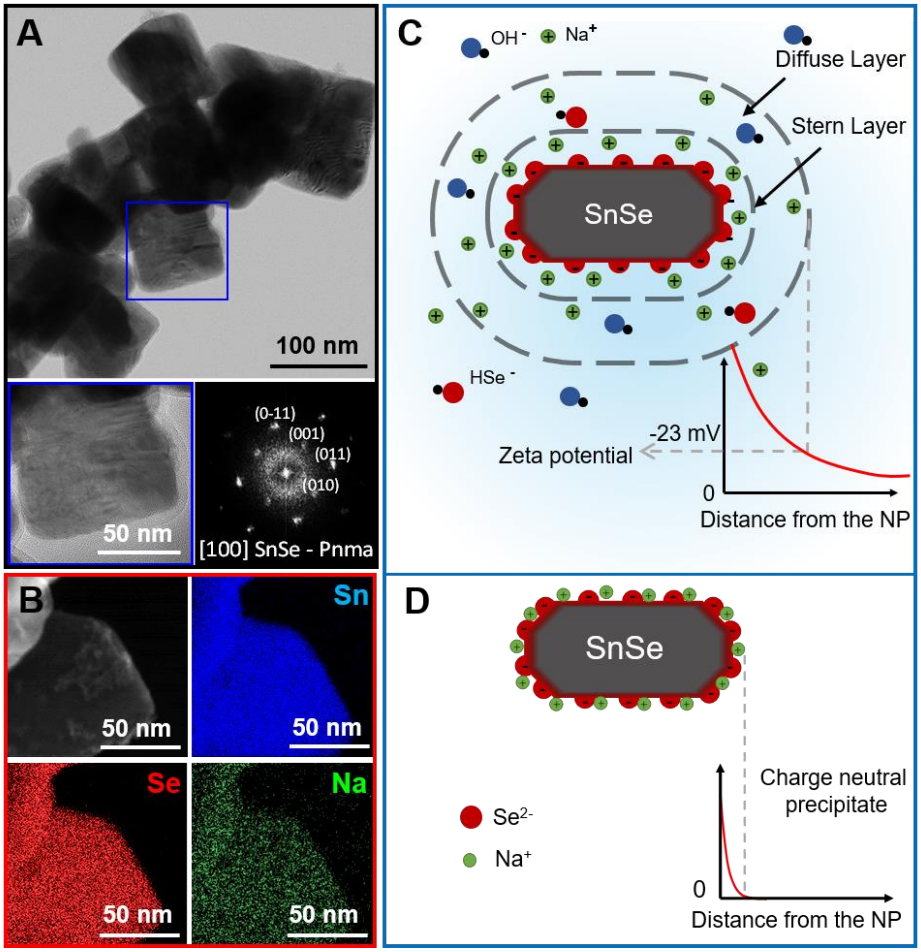

Figure 2. A) Bright-field TEM micrograph of several faceted SnSe NPs, HRTEM micrograph of the rectangular nanoparticle indicated with a blue square, and its corresponding power spectrum (FFT); B) STEM-EDS elemental mapping of Sn (blue), Se (red) and Na (green) for SnSe NPs; C) Schematic representation of the electrical double layer of aSnSe NP in solution; D) Schematic representation of a precipitated NP with Na^+ ions adsorbed to preserve charge neutrality.

4. Pellets microstructure

Compositional analysis with optic emission spectroscopy (ICP-OES, Figure SX) and EDS revealed that the pellets have ca. 2 at% Na content. Beyond the solubility limit, such large Na content is indirect proof that, independently of Na entering the lattice during the NPs synthesis, Na^+ is adsorbed at the NP surface to maintain charge neutrality. We studied pellet's microstructure with atom probe tomography (APT, **Figure 3**) and HRTEM (**Figure 4**) to determine the distribution of Na in the sintered material. Figure 3 shows the 3D distribution of Na in the pellets illustrated by the 2.0 at% Na isoconcentration surfaces; these surfaces are

analogous to contour plots such as altitude in a terrain and highlight the areas where the concentration of Na is ≥2 at%.[61] Na in the pellets is distributed in four different environments: i) within the grains; ii) at dislocations; iii) forming grain boundary complexions,[21] and iv) in nanoprecipitates (Figure 3).

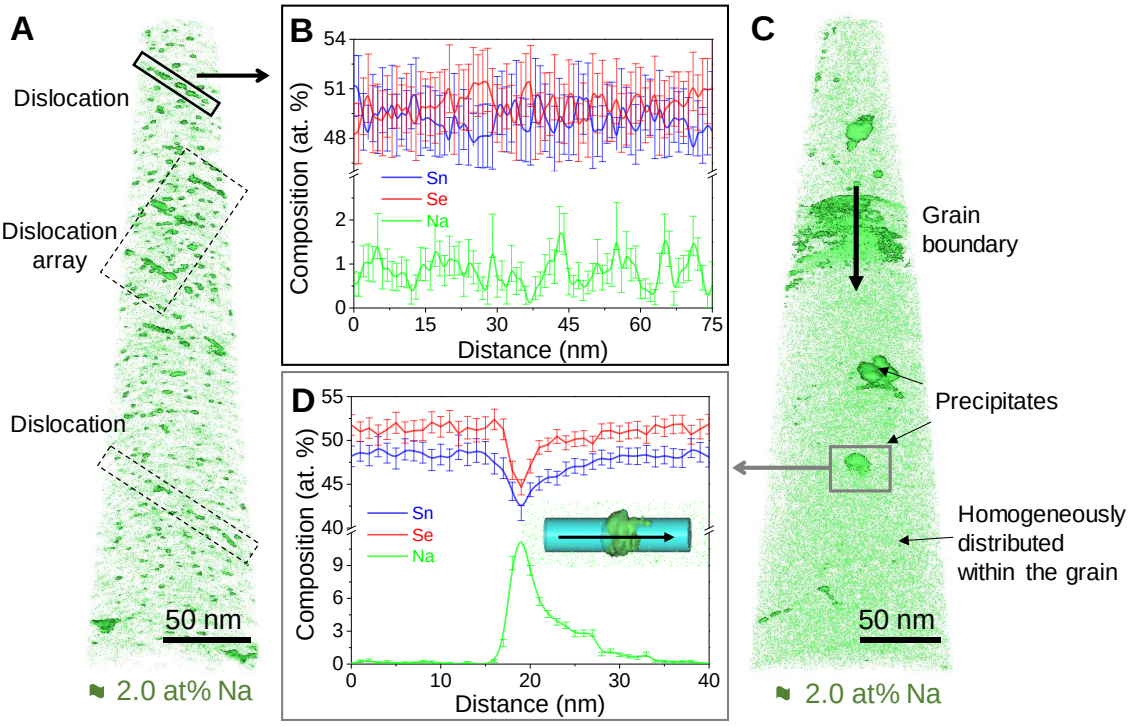

Figure 3. APT of a Na-containing SnSe pellet. A) 3D distribution of Na^+ showing multiple dislocations highlighted by the Na-2.0 at. % isocomposition surface; B) 1D composition profile across a grain dislocation; C) 3D distribution of Na^+ in the same pellet showing Na-rich precipitates; D) 1D composition profile across a precipitate.

The characterizations prove that Na is an involuntary impurity of the NPs, and therefore of the final material when present in the reaction mixture. Hence, to evaluate the effect of Na in the processing and the transport properties of the material, we developed a new synthetic route to obtain Na-free SnSe NPs. In our synthesis, we replaced Na^+ for a cation that decomposes during the annealing step. In particular, we used tetramethylammonium salts: Me_4NBH_4 and Me_4NOH, instead of $NaBH_4$ and NaOH. Following the same synthetic and purification process, we obtained pure phase Me_4N-SnSe NPs with comparable characteristics (size and shape) to the ones produced with Na^+ salts, Na-SnSe NPs (Figure S2). XPS characterization of Me_4N-

SnSe NPs revealed N 1s emission peaks which can be assigned to tetramethylammonium (Figure S1 and S3).[62] None of the elemental analysis techniques used detected Na (Figure S3). Similar to Na-SnSe, Me_4N-SnSe NPs show a negative surface charge (zeta-potential = -23 ± 5 mV). Based on the above, we conclude that the charge balancing ions are Me_4N^+ as depicted in the scheme in Figure 4B. We verified the decomposition of adsorbed Me_4N^+ by *in-situ* mass spectrometry analysis (Figure S4), which revealed that the complete desorption of the organic species is achieved at the annealing temperature in accordance with previous works. The XRD patterns corresponding to the Me_4N-SnSe NPs, annealed powder, and final pellet show the same reflection peaks than Na-SnSe (Figure S2).

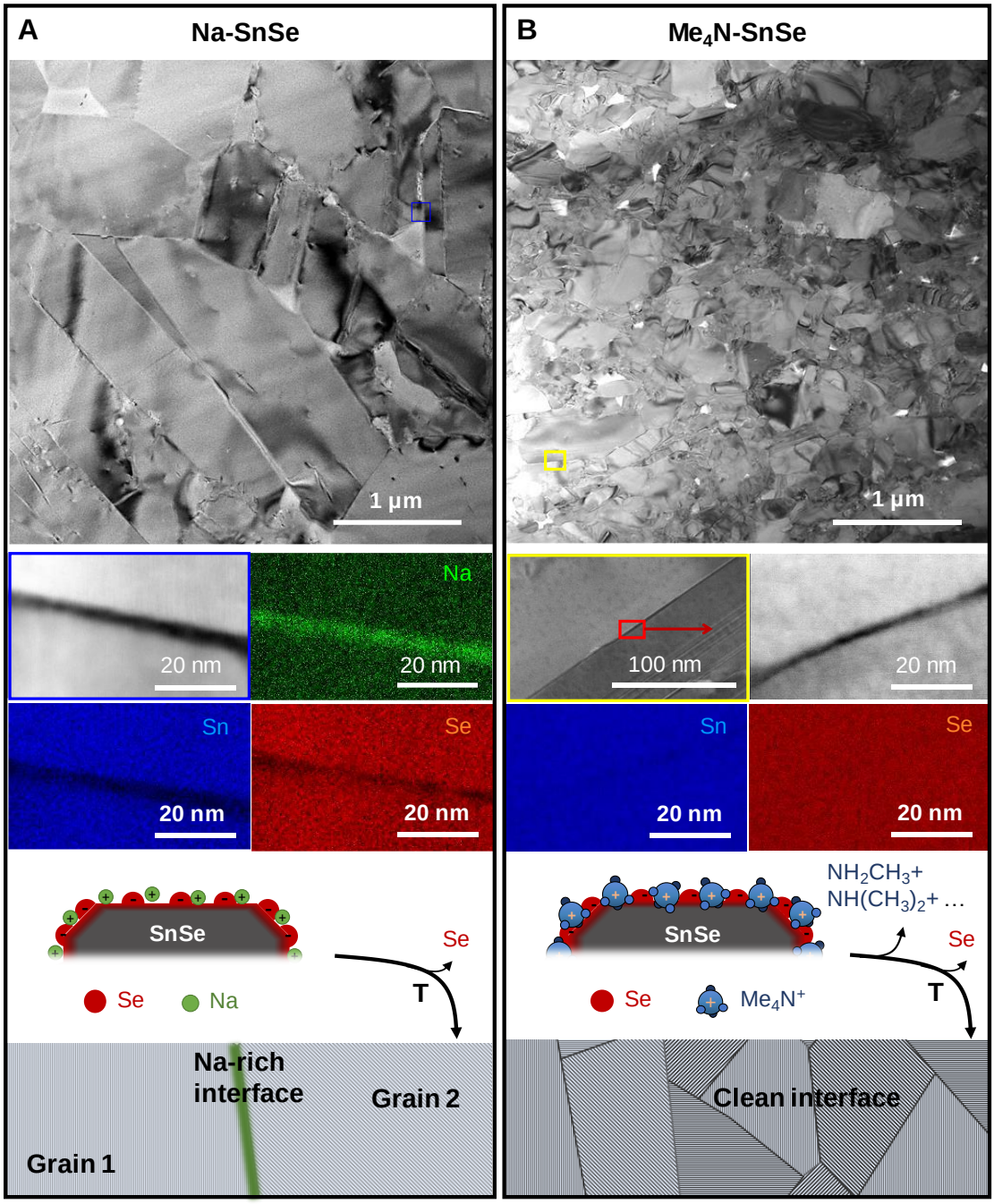

Figure 4. TEM images representing cross-sections of SnSe pellets. General view (top), together with the corresponding EDX elemental mapping of grain boundary (middle), and a scheme of the grain boundary interface in the processing process for two different samples (bottom) of A) Na-SnSe; and B) Me_4N-SnSe.

Although both synthetic strategies yield SnSe NPs with analogous structural properties, the average grain size of the annealed powder and the final pellet is much smaller for Me_4N-SnSe (Figure S2). The average grain size in the Me_4N-SnSe samples after annealing changes from 70 ± 20 nm to 220 ± 100 nm while for the Na-SnSe the grain growth is enhanced (from 150 ±

50 nm to 700 ± 400 nm), showing that the adsorbed ions influence the microstructure development of the samples. We hypothesize that during the thermal processing, the Se-rich surface reacts with Na^+ producing sodium polyselenides (Na_2Se_x) at the NP surface. Furthermore, during the thermal process, the Na_2Se_x phases melt, yielding a liquid phase (Figure S5).[63] Melted polyselenides wet the SnSe NPs providing a capillary force that pulls the grains together.[64] Moreover, the presence of a liquid phase facilitates atomic diffusion between the grains and promotes grain growth. The role of Na_2Se_x promoting crystallization has previously been reported in chalcogenide solar cell absorbers.[65–67] In the case of Me_4N-SnSe, Me_4N^+ decomposes into volatile species upon annealing (Figure S4),[68] and the Se-rich surface does not yield low melting point phases. Since the thermal processing occurs in the absence of a liquid phase, the grain size in the annealed powder and the sintered pellet of Me_4N-SnSe is smaller despite being processed in the same conditions (temperature, pressure, and time).

Both materials yield a large number of dislocations within the grains (Figure S6) which can be correlated to the large amount of Sn vacancies in the NPs and the annealed powder.[69] Upon annealing, these vacancies diffuse, creating vacancy aggregates of lower energy that collapse into dislocations (Figure S6).[70–72] The composition profile along a dislocation line in Figure 3A shows a periodic fluctuation of Na concentration in Na-SnSe, suggesting that the formation of these dislocations is not only an efficient pathway to relax epitaxial strain, but also triggers Na segregation.[73][74] Moreover, the large number of defects in polycrystalline SnSe provides heterogeneous nucleation sites for precipitation,[75–77] explaining the presence of Na-rich precipitates within the grains, at the dislocations, and in grain boundaries in the Na-SnSe sample (Figure 3). However, we could not adequately identify these Na-rich phase exact composition or crystal structure due to its high air sensitivity, ease of oxidation, and instability under the electron beam. Last but not least, HRTEM-EDS analysis across grain boundaries

shows Na-rich grain boundary complexions in Na-SnSe while Me_4N-SnSe has clean interfaces (Figure 4).

5. Transport properties

To evaluate the effects of the Na-SnSe and Me_4N-SnSe distinct microstructure in the transport properties, we measured electrical conductivity and Seebeck coefficient of the respective pellets from room temperature until 833 K (**Figure 5**). The measurements were performed both in the directions parallel and perpendicular to the pressing direction. Here, we exclusively discuss the properties parallel to the pressing direction because the best zT values are obtained along that direction. Measurements in the perpendicular direction show the same trends and can be found in the Supporting Information (Figure S7).

Electrical conductivity of both Na-SnSe and Me_4N-SnSe show a thermally activated behavior, typical of polycrystalline SnSe.[3,25,47,78] However, Na-SnSe has higher electrical conductivity than Me_4N-SnSe over the whole temperature range. Hall effect measurements revealed that this difference is caused by the higher hole concentration of Na-SnSe, ~2.3×10^{19} cm^{-3}, almost three orders of magnitude higher than that of Me_4N-SnSe, ~2.8×10^{16} cm^{-3}. Na is frequently used to dope p-type SnSe[47,48] due to its tendency to sit at Sn^{2+} lattice sites or fill Sn^{2+} vacancies.[79] For Na-SnSe samples, a part of the Na diffused into the matrix (Figure 3), either during the NP synthesis or through the consecutive thermal processes to produce the pellet, and acts as dopant, explaining the high carrier concentration measured.

We observed that the Seebeck coefficient of the Na-SnSe samples is higher than those of polycrystalline samples obtained through melting and annealing, despite the similar charge carrier densities. To illustrate this, we plotted the Seebeck coefficient as a function of charge carrier concentration (Pisarenko plot) at 300 K and compared it with reported experimental data and first-principles calculations using a multiple band model (Figure 5C).[80] Figure 5C reveals that not only our Na-SnSe sample but also many other solution-processed SnSe samples

(half-filled green symbols)[20,25,27,50–52,81] have Seebeck coefficients exceeding the value expected, a tendency not observed in solid-state synthesized SnSe (black open symbols)[40,44–48,82]. The distinct pellets microstructure can explain the high Seebeck coefficients in solution-processed samples. We have shown that Na is inevitably present in the samples if Na salts are used in the reaction due to the nature of this synthetic method. Besides its presence in the matrix as dopant, Na-rich secondary phases are found all over the pellet. The accumulation of Na^+ at the interfaces leads to a positive electric field that induces downwards band bending (Figure 5D), similarly to alkali-doped chalcogenide solar-cell absorbers.[83–85] Such grain boundaries act as an energy barrier, filtering low energy holes and enhancing the Seebeck coefficient.[86,87] In contrast, Me_4N-SnSe has clean grain boundaries, and its Seebeck coefficient behaves as expected by the calculated Pisarenko relation.

Despite the significant difference in the microstructure, both samples have very similar lattice thermal conductivity (Figure S7 and S8). We attribute this to the strong lattice anharmonicity in SnSe as the dominant effect contributing to the thermal conductivity. Overall, we find that the calculated figure of merit is doubled when the NPs are synthesized with Na^+ salts (Figure S8).

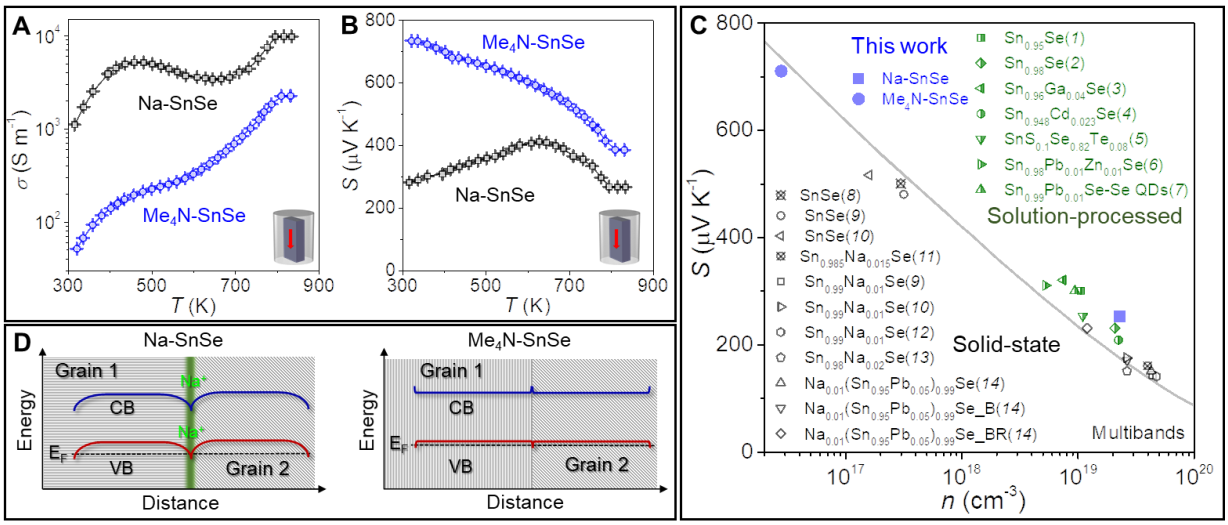

Figure 5. Electronic transport properties of Na-SnSe and Me_4N-SnSe samples measured in the parallel to the pressing direction: A). electrical conductivity, σ; B). Seebeck coefficient, S; C). Seebeck coefficient as a function of Hall carrier concentration at 300 K. Blue solid dots are

experimental data in this work, while green dots and black dots are from solution-processed[20,25,27,50–52,81] and solid-state[43–46,88] (including single crystals[83,89]), respectively. The black solid line was calculated using a multiple band model.[80] D). Scheme showing the band allignment at the grain boundary in Na-SnSe and Me_4N-SnSe.

6. Conclusion

We investigated the role of surface ion adsorbates in polycrystalline SnSe produced from surfactant-free SnSe NPs. We found that when using Na salts in the reaction, Na^+ spectator ions are electrostatically adsorbed on the NPs to preserve charge neutrality once the NPs are removed from the solution. Moreover, Na remains in the material during the annealing and sintering and plays a crucial role in the microstructure evolution and the final material functional properties. In the processed pellets, Na is present within the matrix, in dislocations, precipitates, and forming grain boundary complexions. Due to the tendency of Na^+ to occupy Sn^{2+} sites, Na-SnSe samples exhibit high carrier concentrations. Moreover, the interface between Na-rich segregates and SnSe grains induce downward band bending between grains, leading to charge carrier energy filtering and enhancing the Seebeck coefficient.

For the first time, this work reveals the unavoidable presence of Na^+ species as impurities in solution-processed surfactant-free SnSe and its importance in the transport properties. Furthermore, we explain the rationale behind its presence based on the fundamentals of colloidal science. These findings are relevant because they go beyond the specific system studied. They highlight the importance of evaluating possible unintentional impurities and their origin to i) establish the proper structure-property relationships and ii) redefine synthetic protocols to tune material properties controllably.

An example where the lack of impurity awareness has limited our capability to optimize material properties is for n-type SnSe. Contrary to p-type, where solution methods have reached state-of-the-art thermoelectric performance, for n-type SnSe zT is much lower than xxxxx of

the highest reported value.[90–92] We believe this is correlated to the fact that the synthetic methods used all Na salts to produce SnSe NPs. Hence, when n-type dopants are introduced, the presence of Na^+, up to now unknown, establishes a pinning problem (coexistence of both types of dopants).

7. Experimental Section

SnSe NPs synthesis: SnSe NPs were prepared following a procedure previously reported by Han et al.[31] with slight modifications. In a typical synthesis, $NaBH_4$ (160 mmol, 98%, Fisher Scientific) was first dissolved in 400 ml deionized water, and then Se powder (80 mmol, 100 mesh, ≥99.5%, Sigma-Aldrich) was slowly added into the solution. Stirring should be avoided during this step due to the strong evolution of hydrogen gas. Once the bubbling finished, stirring was resumed under Ar flow until the solution became transparent indicating the complete reduction of Se. In parallel, NaOH (750 mmol, 98% Fisher Scientific) and $SnCl_2 \cdot 2H_2O$ (72 mmol, 98%, Fisher Scientific) were mixed with 360 ml of deionized water. The mixture was stirred at room temperature under Ar flow until complete dissolution. At this point, the solution was heated under reflux to its boiling point (ca. 101.3 °C). The freshly prepared selenide solution was rapidly injected into the boiling Sn (II) solution, and the temperature dropped to ~70 °C. Upon injection, the reaction mixture turned black indicating the NP formation. The temperature was allowed to recover to 101.3 °C and maintained at this temperature for 2 h. To purify the as-synthetized NPs, the mixture was decanted, and the transparent supernatant was carefully discarded. The remaining crude mixture (*ca.* 120 ml) was transferred into 3 centrifuge tubes. The NPs were purified by 3 precipitation/re-dispersion cycles with deionized water and ethanol alternatively. In the first cycle, the fresh deionized water was added into the crude solution by centrifugation at 6000 rpm for 1 min. Then, ethanol was used to redisperse the particles and the solution was centrifuged at 8000 rpm for 5 min. In the second cycle, deionized water was added to solubilize the remaining impurities and NPs

were precipitated by centrifugation at 9000 rpm for 5 min, Afterward, ethanol was employed to re-disperse and precipitate the particles by centrifugation at 8000 rpm for 5 min. These same steps were repeated for a third purification cycle. Washed NPs were dried under vacuum overnight at room temperature and kept in the glovebox for further use.

Me_4N-SnSe NPs: SnSe NPs without Na^+ were produced following the above procedure keeping the molar ratios and using $(CH_3)_4NOH \cdot 5\ H_2O$ (tetramethylammonium hydroxide pentahydrate, 98%, Sigma-Aldrich) and $(CH_3)_4NBH_4$ (tetramethylammonium borohydride, 95%, Sigma-Aldrich) instead of the corresponding Na-reagents.

Bulk nanomaterial sintering: Dried SnSe NPs were annealed at 500 °C for 1 h under a forming gas (95% N_2 + 5% H_2) flow inside a tube furnace with the heating rate of around 10 °C/min. Then, the annealed powder finely grounded with an agate mortar and loaded into a graphite die in a glovebox before being pressed into cylinders (Ø 8.6 mm×12 mm). The process was carried out under vacuum, in an AGUS PECS Spark Plasma Sintering (SPS) System - Model SPS 210Sx applying a pressure of 45 MPa and at temperature of 500 °C for 5 min. The relative densities of the compacted pellets were measured by the Archimedes' method and found to be above 92% of the theoretical value in all samples. From these cylinders, round shape pellets and rectangular bars were cut in two normal directions, *i.e.* parallel to the pressing direction and within the cylinder plane.

Structural and chemical characterization: X-ray diffraction (XRD, 2θ: 20° to 60°; scanning rate: 5°/min) analyses were carried out on a Bruker AXS D8 ADVANCE X-ray diffractometer with Cu–Kα radiation (λ= 1.5406 Å). Size and morphology of initial NPs, annealed nanopowders, sintered pellets were examined by field-emission scanning electron microscopy (SEM) on an Auriga Zeiss operated at 5.0 kV. Composition was investigated by using an Oxford energy dispersive X-ray spectrometer (EDX) attached to the Zeiss Auriga SEM at 15.0

kV. Zeta potential and Zeta Deviations were measured with a Malvern Panalytical Zetasizer Nano (λ = 633 nm) in samples diluted in water (~0.1 mg/ml , pH = 6.5-7.0). The results are the average of 4 measurements with standard deviation <1 and were determined using the Smoluchowski approximation.

HRTEM and STEM studies were conducted using a FEI Tecnai F20 field emission gun microscope operated at 200 kV with a point-to-point resolution of 0.19 nm. Before TEM studies, we prepared a cross-section by cutting it with a diamond saw. The piece obtained was afterward thinned to electron transparency by Focus Ion Beam (FIB) FEI Helios Dual Beam Nanolab. XPS was carried out on a Specs system equipped with a Mg anode XR50 source operating at 250 W and a Phoibos 150 MCD-9 detector (Specs GmbH). The pressure in the analysis chamber was kept below 10^{-7} Pa. Data processing was performed with the CasaXPS program (Casa Software Ltd.).Needle-shaped APT specimens were prepared by a standard "lift-out" method in a SEM/FIB dual-beam focused ion beam microscope (Helios NanoLab 650, FEI). APT measurements were performed on a local electrode atom probe (LEAP4000X Si, Cameca) by applying 10-ps, 5-pJ ultraviolet (wavelength=355 nm) laser pulses. The pulse repetition rate is 200 kHz, and the detection rate is set as 1 ion per 100 pulses on average. The measurement base temperature of specimen is 30 K to minimize surface migration. The ion flight path is 160 mm in our system. The detection efficiency of this LEAP is 50% owing to the open area of the microchannel plates. APT data were processed with the commercial software package IVAS 3.8.0.

Thermoelectric characterization: Seebeck coefficients were measured by using a static DC method. Electrical resistivity data was obtained by a standard four-probe method. Seebeck coefficient and electrical resistivity were measured simultaneously in an LSR-3 LINSEIS system between room temperature and 833 K, under He atmosphere. 3 up and down

measurements were taken. Taking into account the system accuracy and the measurement precision, we estimate an error of *ca.* 4 % in the measurement of the electrical conductivity and Seebeck coefficient, respectively. The thermal conductivity was calculated by $\kappa = \lambda C_p \rho$, where λ is the thermal diffusivity, C_p is the heat capacity, and ρ is the mass density of the specimen. An LFA 1000 LINSEIS was used to determine the thermal diffusivities (λ) of the samples by the Laser Flash method with an estimated error of *ca.* 2.4 %. The constant pressure heat capacity (C_p) was estimated from empirical formula by the Dulong–Petit limit (3R law), and the density (ρ) values were measured using the Archimedes' method. To avoid cluttering the plots, error bars were not included in the figures. Room temperature Hall charge carrier concentrations (n_H) were measured with the Van der Pauw method using a magnetic field of 0.6 T (ezHEMS, NanoMagnetics). Values provided correspond to the average of 6 measurements, from which an error of *ca.* 15% was estimated.

Supporting Information
Supporting Information is available from the Wiley Online Library.

Acknowledgements
This work was financially supported by IST. AustriaYL acknowledges funding from the European Union's Horizon 2020 research and innovation program under the Marie Sklodowska-Curie grant agreement No. 754411. M.C. has received funding from the European Union's Horizon 2020 research and innovation programme under the Marie Skłodowska-Curie Grant Agreement No. 665385.
SIEMENS
CHENG..MEINER

Received: ((will be filled in by the editorial staff))
Revised: ((will be filled in by the editorial staff))
Published online: ((will be filled in by the editorial staff))

References

[1] S. Ortega, M. Ibáñez, Y. Liu, Y. Zhang, M. V Kovalenko, D. Cadavid, A. Cabot, *Chem. Soc. Rev.* **2017**, *46*, 3510.

[2] A. Zevalkink, D. M. Smiadak, J. L. Blackburn, A. J. Ferguson, M. L. Chabinyc, O. Delaire, J. Wang, K. Kovnir, J. Martin, L. T. Schelhas, T. D. Sparks, S. D. Kang, M. T. Dylla, G. J. Snyder, B. R. Ortiz, E. S. Toberer, *Appl. Phys. Rev.* **2018**, *5*, 21303.

[3] S. Chandra, K. Biswas, **2019**, *141*, 6141.

[4] M. Ibáñez, R. Zamani, W. Li, D. Cadavid, S. Gorsse, N. A. Katcho, A. Shavel, A. M. López, J. Ramon Morante, J. Arbiol, A. Cabot, *Chem. Mater.* **2012**, *24*, 4615.

[5] M. Ibáñez, Z. Luo, A. Genç, L. Piveteau, S. Ortega, D. Cadavid, O. Dobrozhan, Y. Liu, M. Nachtegaal, M. Zebarjadi, J. Arbiol, M. V Kovalenko, A. Cabot, *Nat. Commun.* **2016**, *7*, 10766.

[6] Z. Hens, J. De Roo, *J. Am. Chem. Soc.* **2020**, *142*, 15627.

[7] S. H. Park, S. Jo, B. Kwon, F. Kim, H. W. Ban, J. E. Lee, D. H. Gu, S. H. Lee, Y. Hwang, J.-S. Kim, D.-B. Hyun, S. Lee, K. J. Choi, W. Jo, J. S. Son, *Nat. Commun.* **2016**, *7*, 13403.

[8] S. Jo, S. Choo, F. Kim, S. H. Heo, J. S. Son, *Adv. Mater.* **2019**, *31*, 1804930.

[9] Y. Liu, Y. Zhang, S. Ortega, M. Ibáñez, K. Ho Lim, A. Grau-Carbonell, S. Martí-Sánchez, K. Ming Ng, J. Arbiol, M. V. Kovalenko, D. Cadavid, A. Cabot, *Nano Lett.* **2018**, *18*, 2557.

[10] In *Surf. Chem. Colloid. Nanocrystals*, The Royal Society Of Chemistry, **2021**, pp. 1–46.

[11] A. Heuer-Jungemann, N. Feliu, I. Bakaimi, M. Hamaly, A. Alkilany, I. Chakraborty, A. Masood, M. F. Casula, A. Kostopoulou, E. Oh, K. Susumu, M. H. Stewart, I. L. Medintz, E. Stratakis, W. J. Parak, A. G. Kanaras, *Chem. Rev.* **2019**, *119*, 4819.

[12] M. Ibáñez, R. Zamani, S. Gorsse, J. Fan, S. Ortega, D. Cadavid, J. Ramon Morante, J. Arbiol, A. Cabot, *ACS Nano* **2013**, *7*, 2573.

[13] M. Cargnello, C. Chen, B. T. Diroll, V. V. T. Doan-Nguyen, R. J. Gorte, C. B. Murray, *J. Am. Chem. Soc.* **2015**, *137*, 6906.

[14] P. Mohapatra, S. Shaw, D. Mendivelso-Perez, J. M. Bobbitt, T. F. Silva, F. Naab, B. Yuan, X. Tian, E. A. Smith, L. Cademartiri, *Nat. Commun.* **2017**, *8*, 2038.

[15] M. Ibáñez, R. J. Korkosz, Z. Luo, P. Riba, D. Cadavid, S. Ortega, A. Cabot, M. G. Kanatzidis, *J. Am. Chem. Soc.* **2015**, *137*, 4046.

[16] M. Scheele, N. Oeschler, K. Meier, A. Kornowski, C. Klinke, H. Weller, *Adv. Funct. Mater.* **2009**, *19*, 3476.

[17] M. Ibáñez, A. Genç, R. Hasler, Y. Liu, O. Dobrozhan, O. Nazarenko, M. De La Mata, J. Arbiol, A. Cabot, M. V. Kovalenko, *ACS Nano* **2019**, *13*, 6572.

[18] M. Ibáñez, R. Hasler, A. Genç, Y. Liu, B. Kuster, M. Schuster, O. Dobrozhan, D. Cadavid, J. Arbiol, A. Cabot, M. V. Kovalenko, *J. Am. Chem. Soc.* **2019**, *141*, 8025.

[19] J. S. Son, H. Zhang, J. Jang, B. Poudel, A. Waring, L. Nally, D. V. Talapin, *Angew. Chemie - Int. Ed.* **2014**, *53*, 7466.

[20] X. Lou, S. Li, X. Chen, Q. Zhang, H. Deng, J. Zhang, D. Li, X. Zhang, Y. Zhang, H. Zeng, G. Tang, *ACS Nano* **2021**, *0*, DOI 10.1021/acsnano.1c01469.

[21] G. Han, S. R. Popuri, H. F. Greer, R. Zhang, L. Ferre-Llin, J. W. G. Bos, W. Zhou, M. J. Reece, D. J. Paul, A. R. Knox, D. H. Gregory, *Chem. Sci.* **2018**, *9*, 3828.

[22] S. Li, X. Lou, X. Li, J. Zhang, D. Li, H. Deng, J. Liu, G. Tang, *Chem. Mater.* **2020**, *32*, 9761.

[23] G. Tang, W. Wei, J. Zhang, Y. Li, X. Wang, G. Xu, C. Chang, Z. Wang, Y. Du, L. D. D. Zhao, **2016**, *138*, 13647.

[24] M. Li, Y. Liu, Y. Zhang, X. Han, T. Zhang, Y. Zuo, C. Xie, K. Xiao, J. Arbiol, J. Llorca, M. Ibáñez, J. Liu, A. Cabot, *ACS Nano* **n.d.**, *15*, 4967.

[25] W. Wei, C. Chang, T. Yang, J. Liu, H. Tang, J. Zhang, Y. Li, F. Xu, Z. Zhang, J.-F. F. Li, G. Tang, *J. Am. Chem. Soc.* **2018**, *140*, 499.

[26] Y. Gong, C. Chang, W. Wei, J. Liu, W. Xiong, S. Chai, D. Li, J. Zhang, G. Tang, *Scr. Mater.* **2018**, *147*, 74.

[27] J. Liu, P. Wang, M. Wang, R. Xu, J. Zhang, J. Liu, D. Li, N. Liang, Y. Du, G. Chen, G. Tang, *Nano Energy* **2018**, *53*, 683.

[28] X. Shi, W. Liu, A. Wu, V. T. Nguyen, H. Gao, Q. Sun, R. Moshwan, J. Zou, Z. Chen, *InfoMat* **2020**, *2*, 1201.

[29] X. Shi, Z. G. Chen, W. Liu, L. Yang, M. Hong, R. Moshwan, L. Huang, J. Zou, *Energy Storage Mater.* **2018**, *10*, 130.

[30] Y. Min, J. W. Roh, H. Yang, M. Park, S. Il Kim, S. Hwang, S. M. Lee, K. H. Lee, U. Jeong, *Adv. Mater.* **2013**, *25*, 1425.

[31] G. Han, S. R. Popuri, H. F. Greer, J. W. G. Bos, W. Zhou, A. R. Knox, A. Montecucco, J. Siviter, E. A. Man, M. MacAuley, D. J. Paul, W. G. Li, M. C. Paul, M. Gao, T. Sweet, R. Freer, F. Azough, H. Baig, N. Sellami, T. K. Mallick, D. H. Gregory, *Angew. Chemie - Int. Ed.* **2016**, *55*, 6433.

[32] X. Shi, K. Zheng, M. Hong, W. Liu, R. Moshwan, Y. Wang, X. Qu, Z. G. Chen, J. Zou, *Chem. Sci.* **2018**, *9*, 7376.

[33] H. Wang, X. Liu, B. Zhang, L. Huang, M. Yang, X. Zhang, H. Zhang, G. Wang, X. Zhou, G. Han, *Chem. Eng. J.* **2020**, *393*, 124763.

[34] C. Han, Z. Li, G. Q. (Max) Lu, S. Xue Dou, *Nano Energy* **2015**, *15*, 193.

[35] L.-D. Zhao, C. Chang, G. Tan, M. G. Kanatzidis, *Energy Environ. Sci.* **2016**, *9*, 3044.

[36] Z. G. Chen, X. Shi, L. D. Zhao, J. Zou, *High-Performance SnSe Thermoelectric Materials: Progress and Future Challenge*, Elsevier Ltd, **2018**.

[37] A. Banik, S. Roychowdhury, K. Biswas, *Chem. Commun.* **2018**, *54*, 6573.

[38] W. Shi, M. Gao, J. Wei, J. Gao, C. Fan, E. Ashalley, H. Li, Z. Wang, *Adv. Sci.* **2018**, *5*, 1700602.

[39] X.-L. L. Shi, X. Tao, J. Zou, Z.-G. G. Chen, *Adv. Sci.* **2020**, *n/a*, 1902923.

[40] L. D. Zhao, S. H. Lo, Y. Zhang, H. Sun, G. Tan, C. Uher, C. Wolverton, V. P. Dravid, M. G. Kanatzidis, *Nature* **2014**, *508*, 373.

[41] C. Chang, M. Wu, D. He, Y. Pei, C. F. Wu, X. Wu, H. Yu, F. Zhu, K. Wang, Y. Chen, L. Huang, J. F. Li, J. He, L. D. Zhao, *Science (80-.).* **2018**, *360*, 778.

[42] R. Guo, X. Wang, Y. Kuang, B. Huang, *Phys. Rev. B* **2015**, *92*, 115202.

[43] Y. Xiao, C. Chang, Y. Pei, D. Wu, K. Peng, X. Zhou, S. Gong, J. He, Y. Zhang, Z. Zeng, L.-D. Zhao, *Phys. Rev. B* **2016**, *94*, 125203.

[44] Y. K. Lee, Z. Luo, S. P. Cho, M. G. Kanatzidis, I. Chung, *Joule* **2019**, *3*, 719.

[45] Y. Luo, S. Cai, X. Hua, H. Chen, Q. Liang, C. Du, Y. Zheng, J. Shen, J. Xu, C.

Wolverton, V. P. Dravid, Q. Yan, M. G. Kanatzidis, *Adv. Energy Mater.* **2019**, *9*, 1803072.

[46] Z.-H. Ge, D. Song, X. Chong, F. Zheng, L. Jin, X. Qian, L. Zheng, R. E. Dunin-Borkowski, P. Qin, J. Feng, L.-D. Zhao, *J. Am. Chem. Soc.* **2017**, *139*, 9714.

[47] T. R. Wei, G. Tan, X. Zhang, C. F. Wu, J. F. Li, V. P. Dravid, G. J. Snyder, M. G. Kanatzidis, *J. Am. Chem. Soc.* **2016**, *138*, 8875.

[48] E. K. Chere, Q. Zhang, K. Dahal, F. Cao, J. Mao, Z. Ren, *J. Mater. Chem. A* **2016**, *4*, 1848.

[49] M. Li, Y. Liu, Y. Zhang, Y. Zuo, J. Li, K. H. H. Lim, D. Cadavid, K. M. M. Ng, A. Cabot, *Dalton. Trans.* **2019**, *48*, 3641.

[50] X. Shi, Z. G. Chen, W. Liu, L. Yang, M. Hong, R. Moshwan, L. Huang, J. Zou, *Energy Storage Mater.* **2018**, *10*, 130.

[51] R. Xu, L. Huang, J. Zhang, D. Li, J. Liu, J. Liu, J. Fang, M. Wang, G. Tang, *J. Mater. Chem. A* **2019**, *7*, 15757.

[52] X. Shi, A. Wu, T. Feng, K. Zheng, W. Liu, Q. Sun, M. Hong, S. T. Pantelides, Z.-G. Chen, J. Zou, *Adv. Energy Mater.* **2019**, *9*, 1803242.

[53] X. Liu, J. Xiao, H. Peng, X. Hong, K. Chan, J. K. Nørskov, *Nat. Commun.* **2017**, *8*, 1.

[54] X. Shi, A. Wu, W. Liu, R. Moshwan, Y. Wang, Z.-G. G. G. Chen, J. Zou, *ACS Nano* **2018**, *12*, 11417.

[55] M. Hong, Z. G. Chen, L. Yang, T. C. Chasapis, S. D. Kang, Y. Zou, G. J. Auchterlonie, M. G. Kanatzidis, G. J. Snyder, J. Zou, *J. Mater. Chem. A* **2017**, *5*, 10713.

[56] M. Yarema, O. Yarema, W. M. M. Lin, S. Volk, N. Yazdani, D. Bozyigit, V. Wood, *Chem. Mater.* **2017**, *29*, 796.

[57] K. Nakano, T. Sato, M. Tazaki, M. Takagi, **2000**, DOI 10.1021/la990688x.

[58] S. C. Riha, D. C. Johnson, A. L. Prieto, *J. Am. Chem. Soc.* **2011**, *133*, 1383.

[59] D. Zhu, A. Tang, Q. Kong, B. Zeng, C. Yang, F. Teng, *J. Phys. Chem. C* **2017**, *121*, DOI 10.1021/acs.jpcc.7b03826.

[60] D. Zhu, L. Wang, Z. Liu, A. Tang, *Appl. Surf. Sci.* **2020**, *509*, 145327.

[61] O. C. Hellman, J. A. Vandenbroucke, J. Rüsing, D. Isheim, D. N. Seidman, *Microsc. Microanal.* **2000**, *6*, 437.

[62] H. Konno, Y. Yamamoto, *Bull. Chem. Soc. Jpn.* **1987**, *60*, 2561.

[63] J. Sangster, A. D. D. Pelton, *The Na-Se (Sodium-Selenium) System*, ASM International, **1997**.

[64] S.-J. L. Kang, *Sintering: Densification, Grain Growth, and Microstructure*, Butterworth-Heinemann, Oxford, **2005**.

[65] C. M. Sutter-Fella, J. A. Stückelberger, H. Hagendorfer, F. La Mattina, L. Kranz, S. Nishiwaki, A. R. Uhl, Y. E. Romanyuk, A. N. Tiwari, *Chem. Mater.* **2014**, *26*, 1420.

[66] D. Braunger, D. Hariskos, G. Bilger, U. Rau, H. W. Schock, *Thin Solid Films* **2000**, *361*, 161.

[67] M. Johnson, S. V. Baryshev, E. Thimsen, M. Manno, X. Zhang, I. V. Veryovkin, C.

Leighton, E. S. Aydil, *Energy Environ. Sci.* **2014**, *7*, 1931.

[68] W. K. Musker, *J. Am. Chem. Soc.* **1964**, *86*, 960.

[69] P. M. Anderson, J. P. Hirth, J. Lothe, *Theory of Dislocations*, Cambridge University Press, Cambridge, **2017**.

[70] K. V Ravi, *Metall. Trans.* **1972**, *3*, 1311.

[71] Z. Chen, B. Ge, W. Li, S. Lin, J. Shen, Y. Chang, R. Hanus, G. J. Snyder, Y. Pei, *Nat. Commun.* **2017**, *8*, 13828.

[72] Z. Chen, Z. Jian, W. Li, Y. Chang, B. Ge, R. Hanus, J. Yang, Y. Chen, M. Huang, G. J. Snyder, Y. Pei, *Adv. Mater.* **2017**, *29*, 1606768.

[73] M. Legros, G. Dehm, E. Arzt, T. J. Balk, *Science (80-.).* **2008**, *319*, 1646 LP.

[74] Y. Yu, S. Zhang, A. M. Mio, B. Gault, A. Sheskin, C. Scheu, D. Raabe, F. Zu, M. Wuttig, Y. Amouyal, O. Cojocaru-Mirédin, *ACS Appl. Mater. Interfaces* **2018**, *10*, 3609.

[75] S. A. Yamini, T. Ikeda, A. Lalonde, Y. Pei, S. X. Dou, G. J. Snyder, *J. Mater. Chem. A* **2013**, *1*, 8725.

[76] J. He, I. D. Blum, H.-Q. Wang, S. N. Girard, J. Doak, L.-D. Zhao, J.-C. Zheng, G. Casillas, C. Wolverton, M. Jose-Yacaman, D. N. Seidman, M. G. Kanatzidis, V. P. Dravid, *Nano Lett.* **2012**, *12*, 5979.

[77] S. A. Yamini, D. R. G. Mitchell, Z. M. Gibbs, R. Santos, V. Patterson, S. Li, Y. Z. Pei, S. X. Dou, G. Jeffrey Snyder, *Adv. Energy Mater.* **2015**, *5*, 1501047.

[78] Y. K. Lee, K. Ahn, J. Cha, C. Zhou, H. S. Kim, G. Choi, S. I. Chae, J. H. Park, S. P. Cho, S. H. Park, Y. E. Sung, W. B. Lee, T. Hyeon, I. Chung, *J. Am. Chem. Soc.* **2017**, *139*, 10887.

[79] Y. Zhou, W. Li, M. Wu, L.-D. Zhao, J. He, S.-H. Wei, L. Huang, *Phys. Rev. B* **2018**, *97*, 245202.

[80] G. Shi, E. Kioupakis, *J. Appl. Phys.* **2015**, *117*, 065103.

[81] L. Huang, G. Han, B. Zhang, D. H. Gregory, *J. Mater. Chem. C* **2019**, *7*, 7572.

[82] L. D. Zhao, G. Tan, S. Hao, J. He, Y. Pei, H. Chi, H. Wang, S. Gong, H. Xu, V. P. Dravid, C. Uher, G. J. Snyder, C. Wolverton, M. G. Kanatzidis, *Science (80-.).* **2016**, *351*, 141.

[83] J. B. Li, V. Chawla, B. M. Clemens, *Adv. Mater.* **2012**, *24*, 720.

[84] Y. Yan, C. S. Jiang, R. Noufi, S. H. Wei, H. R. Moutinho, M. M. Al-Jassim, *Phys. Rev. Lett.* **2007**, *99*, 235504.

[85] C. S. Jiang, R. Noufi, J. A. AbuShama, K. Ramanathan, H. R. Moutinho, J. Pankow, M. M. Al-Jassim, *Appl. Phys. Lett.* **2004**, *84*, 3477.

[86] C. Gayner, Y. Amouyal, *Adv. Funct. Mater.* **2019**, DOI 10.1002/adfm.201901789.

[87] J. Martin, L. Wang, L. Chen, G. S. Nolas, *Phys. Rev. B* **2009**, *79*, 115311.

[88] T. R. Wei, G. Tan, C. F. Wu, C. Chang, L. D. Zhao, J. F. Li, G. J. Snyder, M. G. Kanatzidis, *Appl. Phys. Lett.* **2017**, *110*, 053901.

[89] X. Shi, X. Tao, J. Zou, Z. Chen, *Adv. Sci.* **2020**, *7*, 1902923.

[90] X.-L. Shi, K. Zheng, W.-D. Liu, Y. Wang, Y.-Z. Yang, Z.-G. Chen, J. Zou, *Adv. Energy Mater.* **2018**, *8*, 1800775.

[91] S. Chandra, A. Banik, K. Biswas, *ACS Energy Lett.* **2018**, *3*, 1153.

[92] Z.-H. Ge, Y. Qiu, Y.-X. Chen, X. Chong, J. Feng, Z.-K. Liu, J. He, *Adv. Funct. Mater.* **2019**, *29*, 1902893.